ATMOSPHERIC SCIENCE

Optimal choice of proxy for cloud condensation nuclei reduces uncertainty in aerosol-cloud-climate forcing

Hailing Jia[1]*, Johannes Quaas[2], Willem Kroese[3], Bastiaan van Diedenhoven[1], Edward Gryspeerdt[4], Christoph Böhm[5], Karoline Block[2], Otto Hasekamp[1]

Aerosol-cloud interactions (ACI) remain the largest uncertainty in anthropogenic climate forcings. Observation-based estimates of instantaneous radiative forcing from ACI (RF_{aci}; the Twomey effect) rely on the choice of aerosol quantities as proxies for cloud condensation nuclei (CCN) concentrations, which differ in their ability to represent cloud-base CCN and data accuracy. Using diverse observations and aerosol-climate models, we evaluate the utility of different proxies with two independent approaches. Both approaches reveal that surface CCN exhibits the smallest bias in predicting RF_{aci} (+5%), followed by aerosol index, surface sulfate and column CCN with similar biases of +25%, while aerosol optical depth and column sulfate show the largest biases (−60% and +92%). Constraining RF_{aci} with the optimal proxy reduces uncertainty from 66 to 43%, yielding a less negative RF_{aci} (−1.0 W m^{-2}) than the unconstrained case (−1.2 W m^{-2}). Our findings highlight the crucial role of proxy constraint in reconciling and improving RF_{aci} estimates.

INTRODUCTION

The change in reflected shortwave radiation from the preindustrial (PI) era to the present day (PD) due to increased anthropogenic aerosols is the most uncertain component of the anthropogenic radiative forcing, with much of this uncertainty stemming from aerosol-cloud interactions (ACIs) (*1*). By serving as cloud condensation nuclei (CCN), aerosols increase cloud droplet number concentration (N_d), which in turn increase cloud brightness, leading to instantaneous radiative forcing due to ACI (RF_{aci}; also known as the Twomey effect) (*2*). The altered N_d subsequently triggers rapid adjustments to cloud cover and liquid water path (*3*, *4*), which, together with RF_{aci}, constitute the effective radiative forcing due to ACI (ERF_{aci}). The rapid adjustments are very uncertain in both sign and magnitude (*5*–*8*), but approximately scale with the anthropogenic perturbation to N_d ($\Delta\ln N_d$) and RF_{aci} (*9*, *10*). This study will focus on providing observational constraints on $\Delta\ln N_d$ and RF_{aci}.

Because of the lack of PI observations of cloud properties, $\Delta\ln N_d$ (hence RF_{aci}) is commonly inferred from anthropogenic perturbation to aerosol ($\Delta\ln A$, with A representing aerosol amount) that is typically from a pair of PD-PI aerosol-climate simulations, together with N_d susceptibility to aerosols $\left(\beta_{A,PD} = \frac{d\ln N_d}{d\ln A}\right)$ derived from the PD spatiotemporal variability of aerosol and cloud properties observed from satellites, assuming a linear $\ln A$–$\ln N_d$ relationship (*11*–*13*)

$$\Delta\ln N_d = \beta_{A,PD}\Delta\ln A \tag{1}$$

Recent studies have found a reduced $\Delta\ln N_d$ at high aerosol concentrations, indicating a nonlinear $\ln A$–$\ln N_d$ behavior (*14*, *15*), which can be taken into account by other nonlinear approaches, albeit requiring more comprehensive formulations (*14*, *16*) (see Discussion). The total uncertainty in $\Delta\ln N_d$ arises from (as also illustrated in the schematic, Fig. 1): (i) uncertainties in $\beta_{A,PD}$ that are associated with methodologies for sampling data and calculating $\beta_{A,PD}$ and measurement errors (a central focus in prior ACI research, but not the focus here), (ii) uncertainties in $\Delta\ln A$ due to uncertainty especially in PI aerosols and heterogeneity of aerosol perturbations (*17*), which rely on the model uncertainty, and (iii) the choice of CCN proxy (i.e., which A to use). Among these, the choice of CCN proxy is particularly important because Eq. 1 assumes that the PD $\beta_{A,PD}$ is indicative of the actual N_d susceptibility to anthropogenic perturbation to A, i.e., the PI-to-PD susceptibility $\beta_{A,PI-PD}\left(\frac{\ln N_{d,PD}-\ln N_{d,PI}}{\ln A_{PD}-\ln A_{PI}}\right)$. In principle, the best choice would be using CCN at the cloud base (CCN_b) because the CCN_b-N_d relationship is least affected by PI-to-PD shifts in aerosol regime (e.g., from coarse- to fine-mode dominated) and vertical distribution (*16*). However, because of the difficulty in measuring CCN_b [typically from in situ observations (*18*)] at the global scale, various proxies such as aerosol optical depth (AOD), aerosol index (AI), sulfate column and surface mass concentrations ($SO4_c$ and $SO4_s$), and column-integrated CCN number concentration (CCN_c) are often used instead (*17*). This leads to a large uncertainty and complicates the reconciliation of disparate RF_{aci} estimates (*19*). Aerosol-type classification by satellites might help to reduce the uncertainty from aerosol regime shifts in regions dominated by a single aerosol type (*20*), although it is less useful for global RF_{aci} estimates because most regions are influenced by mixtures of aerosol types with varying proportions. While these uncertainties have been recognized (*16*, *19*, *21*, *22*), their contributions to the total uncertainty remain unclear, mainly due to a limited selection of proxies and models being considered.

A crucial step forward is to constrain these identified uncertainties. Compared to $\Delta\ln A$ that heavily relies on the model uncertainty, the uncertainty from proxy selection is more readily constrained, but remains challenging. Although remotely sensed AI and CCN_c that carry information of particle size and/or hygroscopicity show advantages over AOD, they still suffer from lack of vertical and horizontal colocations between aerosol and cloud (*23*, *24*). Reanalyzed quantities may help to mitigate this issue but introduce additional uncertainty in data accuracy tied to the host model. Therefore, an objective framework is needed to evaluate the utility of different proxies from various products for diagnosing RF_{aci}.

[1]SRON Space Research Organisation Netherlands, Leiden 2333CA, Netherlands. [2]Leipzig Institute for Meteorology, Leipzig University, Leipzig 04109, Germany. [3]Utrecht University, Utrecht 3584CS, Netherlands. [4]Department of Physics, Imperial College London, London SW72AZ, UK. [5]Institute for Geophysics and Meteorology, University of Cologne, Cologne 50969, Germany.
*Corresponding author. Email: h.jia@sron.nl

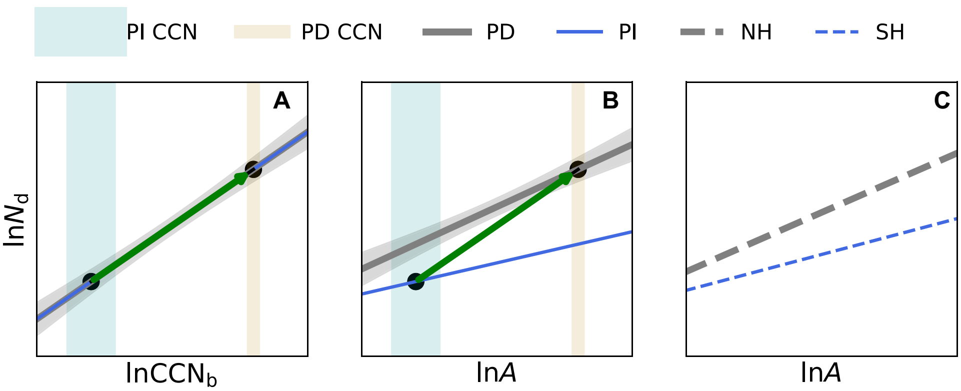

Fig. 1. Schematic illustrating the uncertainty sources in the RF_{aci} estimation from observations, assuming a linear ln *A*–ln N_d relationship. The relationships of (**A**) ln CCN_b–ln N_d and (**B**) ln *A*–ln N_d in the PI (blue line) and PD (gray line) environments, with *A* denoting a CCN proxy (the behavior of AOD as an example here), where the PI-to-PD susceptibility ($\beta_{A,PI-PD}$) is shown as green arrows. The uncertainty in modeled Δln *A* is indicated by vertical shadings, where the light blue and brown shadings represent mean aerosol concentrations in the PI and PD, respectively, with the width indicating the model uncertainty. The uncertainty in determining the PD N_d susceptibility ($\beta_{A,PD}$) from observations is depicted as gray shading. (**C**) Conceptual relationships of ln *A*–ln N_d in the PD Southern Hemisphere (SH, blue dashed line) and Northern Hemisphere (NH, gray dashed line). This illustrates the similarity between the SH-NH and PI-PD contrasts.

In this work, we present two independent approaches to determine the optimal proxies. The first approach uses observed hemispheric contrasts in N_d conditioned on aerosol for different proxies, to assess the dependence of ln *A*–ln N_d relations on aerosol regime. The second approach is based on synthetic experiments using climate simulations from the AeroCom intercomparison (*25*–*27*), to investigate how well $\beta_{A,PD}$ is representative for $\beta_{A,PI-PD}$. On the basis of the optimal CCN proxy selection, we propose a correction term for other proxies that, although they do not perfectly reflect the "true" CCN, can be measured with relatively high accuracy to determine $\beta_{A,PD}$. Furthermore, we use a large variety of different observational products and aerosol-climate models to decompose the RF_{aci} uncertainty into components, including the choice of CCN proxy and modeled Δln *A*. Ultimately, by constraining the proxy-related uncertainty, this study will provide improved observational constraints on both Δln N_d and RF_{aci}, along with a robust uncertainty assessment. Our analysis focuses on marine liquid clouds between 60°S and 60°N due to the limited retrieval quality over land and polar regions.

RESULTS

Observed hemispheric contrasts in N_d conditioned on aerosol

Figure 1 illustrates the idea of making use of the observed hemispheric contrasts in aerosols and clouds to learn about ACIs. Assuming the same meteorology in the PI and PD (a common assumption for diagnosing aerosol forcing), CCN_b would result in same PI and PD aerosol–N_d relationships that are indicative of the PI-to-PD change (Fig. 1A). However, for a proxy whose linkage to CCN_b varies across aerosol regimes, for instance AOD, the larger contribution of coarse-mode aerosols in the PI that are less relevant to N_d yields systematically lower N_d than the PD environment [Fig. 1B, (*16*, *28*)], causing $\beta_{A,PD}$ (gray curve) to deviate from $\beta_{A,PI-PD}$ (green arrow). The extent of deviation, of course, depends on how well a given proxy represents particle size and hygroscopicity at the cloud base. To examine this deviation due to the aerosol regime shift, we use the more pristine Southern Hemisphere (SH) and more polluted Northern Hemisphere (NH) to mimic the PI and PD aerosol environments, respectively [Fig. 1C, (*29*, *30*)]. To ensure the similar meteorological backgrounds, the *k*-means clustering algorithm is applied to separate meteorological regimes (fig. S1 and Materials and Methods). The key hypothesis is that at the same meteorological background and same *A* value, a good CCN proxy should (when observational errors at the same *A* value are similar in both hemispheres) lead to the same N_d in both hemispheres where aerosol regimes are very different.

A metric, $\Delta N_{d|SH-NH|}$, is defined to quantify the hemispheric contrast at fixed *A* values (Materials and Methods). The $\Delta N_{d|SH-NH|}$ for different proxies and different meteorological regimes are shown in Fig. 2. Note that all CCN-relevant proxies in this study, including CCN number concentrations at surface (CCN_s), at cloud base (CCN_b) and column-integrated (CCN_c), are at 0.2% supersaturation. For the interpretation of Fig. 2, we focus on the Copernicus Atmosphere Monitoring Service (CAMS) reanalysis data because it provides most proxy quantities (except for sulfate mass concentration at cloud base, $SO4_b$) and also because in reanalysis data the product errors can be assumed the same in both hemispheres. Another reanalysis product, the Modern-Era Retrospective analysis for Research and Applications version 2 (MERRA-2), shows a very similar behavior as CAMS, although CCN data are missing (blue line in Fig. 2). As anticipated, AOD exhibits the largest $\Delta N_{d|SH-NH|}$ [26%, averaged across the three meteorological clusters 0 to 2 (C0 to C2)], implying the potentially largest deviation of ln *A*–ln N_d relationships between PI and PD. This is followed by sulfate column concentration ($SO4_c$) with a $\Delta N_{d|SH-NH|}$ of ~14%, which better represents CCN-relevant fine-mode aerosols but still lacks vertical colocation. Also, $SO4_c$ is biased as it does not account for other CCN-relevant species that are potentially uncorrelated to the distribution of SO4, such as hydrophilic organic carbon. Proxies that either account for all CCN-relevant species (AI and CCN_c) or provide aerosol information within boundary layer (sulfate surface mass concentration, $SO4_s$) achieve lower $\Delta N_{d|SH-NH|}$ (10 to 11%) compared to $SO4_c$. The $\Delta N_{d|SH-NH|}$ reduces progressively from CCN_c to CCN_s and finally CCN_b, underscoring the importance of having aerosol information at the cloud base. Among all proxies, CCN_b shows the smallest hemispheric contrast in N_d conditioned on aerosol of only ~4%.

When considering all products, the overall conclusion remains consistent (gray line in Fig. 2) despite some variations across different

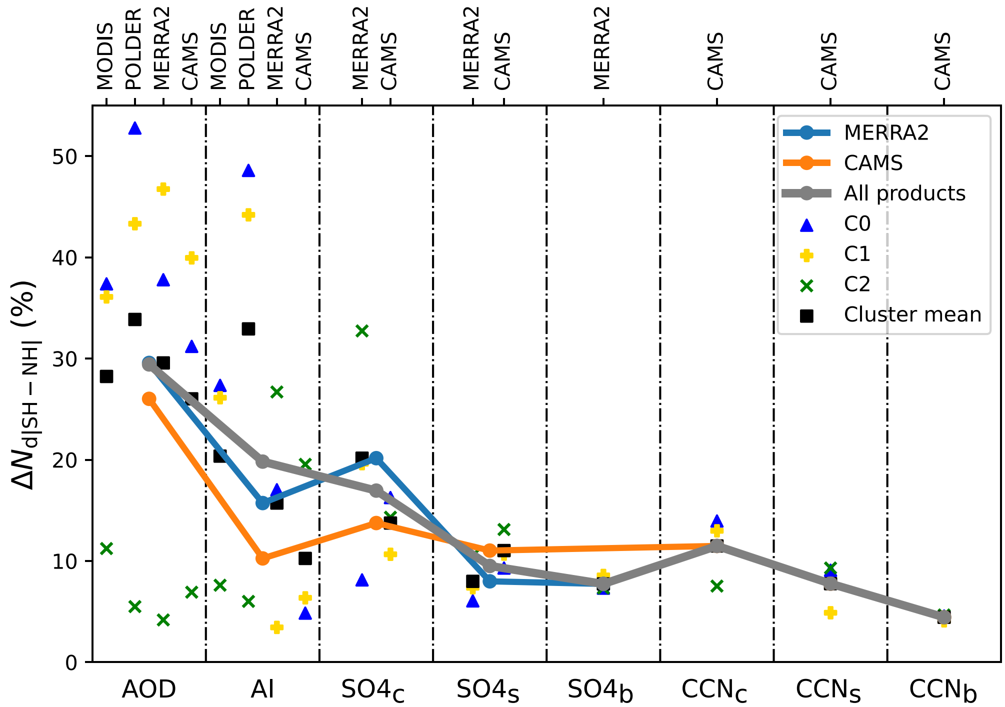

Fig. 2. Hemispheric contrasts in N_d at fixed A values ($\Delta N_{d|SH-NH|}$) for different proxies from various products and different meteorological regimes. $\Delta N_{d|SH-NH|}$ represents the absolute value of relative deviation (in units of %, Eq. 3). Crosses represent $\Delta N_{d|SH-NH|}$ for three meteorological regimes that are relevant for liquid clouds (fig. S1), including C0 (blue), C1 (yellow), and C2 (green). Mean $\Delta N_{d|SH-NH|}$ overall regimes are shown as black squares. Blue and orange curves denote $\Delta N_{d|SH-NH|}$ from MERRA-2 and CAMS products, respectively, while gray curve shows the mean of all products. Note that only oceans within 30°–60° latitude bands are considered here.

products. Compared to reanalysis datasets, satellite products generally lead to a large hemispheric contrast, likely due to different data error characteristics in satellite and reanalysis data. Nevertheless, the hemispheric contrast is smaller in satellite-derived AI compared to AOD, consistent with reanalysis products. Looking at different regimes, which occur with frequencies of 23% for C0, 54% for C1, and 19% for C2, the $\Delta N_{d|SH-NH|}$ behavior appears only in regimes associated with stratocumulus (C0) and trade wind cumulus clouds (C1), but not in the convective cloud-dominated regime (C2), where the strong N_d sink by precipitation veils part of aerosol effects (*31*), and also the N_d retrieval is less reliable for these clouds (*32*).

The result from hemispheric contrasts provides direct observational evidence that incorporating aerosol size, hygroscopicity, and vertical distribution helps to remove the dependency of ln A–ln N_d relationships on aerosol regime, supporting findings from modeling studies (*16*, *23*, *28*). Moreover, the result reveals that there does exist an aerosol quantity in current observation-derived datasets, CAMS CCN_b, that can evidently mitigate, although not completely eliminate, the aerosol-regime dependency issue, owing to the comprehensive aerosol information it includes. The remaining hemispheric contrasts in N_d may be explained by inherent uncertainties in CAMS CCN product (*33*), which warrants further improvement in data quality. Given that CCN_s yields the second-smallest hemispheric contrast, it may serve as a useful alternative when CCN_b data are unavailable (see below).

Synthetic experiments using AeroCom models

Synthetic experiments in a model world have proven to be a useful test bed for evaluating observational approaches for quantifying RF_{aci} (*16*), as the "truth" is known. Building on the synthetic experiments, relative biases in RF_{aci} caused by inadequate proxies were reported by comparing modeled $\Delta \ln N_d$ and diagnosed $\Delta \ln N_d$ using a joint histogram method, with a focus on AOD, AI, CCN_c, and CCN_s (*16*). In this study, we revisit the relative biases in RF_{aci} from a different perspective: $\beta_{A,PD}$ (gray line in Fig. 1) versus $\beta_{A,PI-PD}$ (green arrow in Fig. 1), considering all available proxies. Both $\beta_{A,PD}$ and $\beta_{A,PI-PD}$ are derived through a linear method based on monthly A and N_d from the AeroCom PI and PD simulations, and then used to diagnose the relative bias in RF_{aci} introduced by approximating $\beta_{A,PI-PD}$ with $\beta_{A,PD}$ (δ_{mod}; Materials and Methods). Here, $SO4_b$ and CCN_b are not included due to the lack of cloud-base outputs in the models.

As shown in Fig. 3 (blue squares), CCN_s exhibits the smallest bias (+5%), followed by AI, $SO4_s$, and CCN_c with similar positive biases of ~+25%. In contrast, AOD and $SO4_c$ show the largest biases, with values of −60 and +92%, respectively. With the same chemical composition, the column-integrated proxies ($SO4_c$ and CCN_c) tend to have larger positive biases in RF_{aci} than the surface proxies ($SO4_s$ and CCN_s). This suggests that the biased high $\beta_{A,PD}$ from column-integrated proxies, as reported by (*31*), cannot be fully compensated by their smaller anthropogenic perturbations as previously speculated (*17*). Instead, the co-occurrence of higher $\beta_{A,PD}$ and $\Delta \ln A$ of column-integrated quantities leads to the large positive bias (fig. S6). The lack of vertical information results in an RF_{aci} overestimation of ~70% for SO4 and ~25% for CCN. It is important to note that despite using distinct methodologies, our findings show a strong agreement with the biases reported by (*16*) (orange crosses in Fig. 3), with discrepancies of only 5% for AOD, 13% for AI, 3% for CCN_c, and 14% for CCN_s.

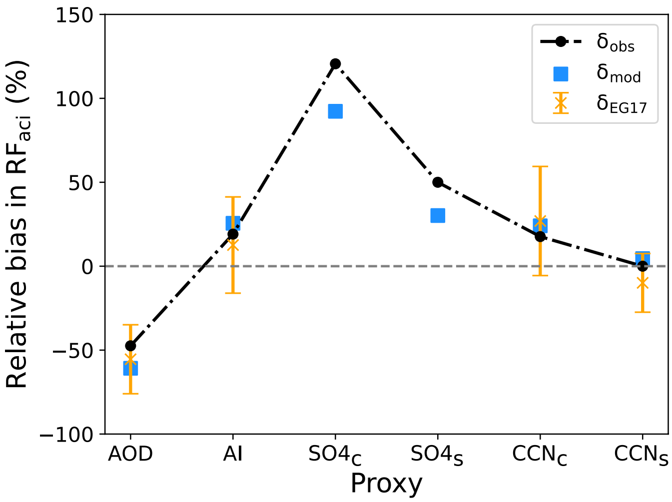

Fig. 3. Comparison of relative biases in RF_{aci} caused by using different CCN proxies estimated using model-based (δ_{mod}) and observational (δ_{obs}) approaches (see Materials and Methods). Another model-based estimate from (*16*) is also shown as a cross-validation (δ_{EG17}), with error bars indicating the intermodel SD. Both δ_{mod} and δ_{EG17} are based on the AeroCom AP2_IND3 models (table S2). As for δ_{obs}, ECHAM-HAM and HadGEM3-A-GLOMAP that provide outputs of all proxies are used, to isolate the effect of proxy selection from differing $\Delta \ln A$ across various models.

This consistency provides a form of cross-validation and strengthens the robustness of the conclusions about the reported RF_{aci} biases here.

What does this bias look like from the observational side? According to both hemispheric contrasts and synthetic experiments, although a slight degradation in CCN_s's utility as a CCN proxy compared to CCN_b, CCN_s still performs satisfactorily in predicting RF_{aci} with a bias under 5%. Therefore, assuming CCN_s would give the true RF_{aci}, the relative bias in observation-based RF_{aci} caused by inadequate proxies (δ_{obs}; Materials and Methods) can be inferred as well (connected black dots in Fig. 3). Figure 3 shows a remarkable agreement between δ_{obs} and δ_{mod}, particularly for AOD, AI, CCN_c, and CCN_s, with discrepancies of only 13, 6, 6, and 5%, respectively, although relatively larger differences are seen for $SO4_c$ (28%) and $SO4_s$ (20%).

It has become clear that three independent lines of evidence from models and observations shown in Fig. 3 converge on the conclusion: CCN_b, but next to it, CCN_s is the best-suited proxy, in agreement with the finding from the hemispheric contrast results. Furthermore, the consistent RF_{aci} biases estimated from different methods reinforces our confidence in using the relative biases presented here as "emergent scaling" factors, to adjust RF_{aci} estimated from any inadequate proxy to a plausible level. This is particularly useful for the proxies that have potential to be observed directly from space with high accuracy but lack some essential aerosol information.

It is also interesting to note that the rankings of "good" proxies, as informed by the hemispheric contrasts (Fig. 2) and RF_{aci} biases (Fig. 3), do not always agree, especially for $SO4_c$ and $SO4_s$, which exhibit moderate hemispheric contrasts yet very high RF_{aci} biases. This discrepancy occurs because the former only reflects the bias related to $\beta_{A,PD}$ deviation, whereas the latter additionally incorporates the role of $\Delta \ln A$ (Eq. 1) as a modulating factor. Depending on the nature of proxies, $\Delta \ln A$ acts to either amplify or attenuate the bias related to the $\beta_{A,PD}$ deviation. For $SO4_c$ and $SO4_s$ that are primarily driven by anthropogenic fine-mode aerosols, the very high $\Delta \ln A$ (~0.55; figs. S2 and S6) acts to substantially amplify the bias related to β as seen in the hemispheric contrast. This highlights the importance of accounting for the role of $\Delta \ln A$ and its associated uncertainty in RF_{aci} estimates.

Decomposing and constraining RF_{aci} uncertainty

Using regional $\beta_{A,PD}$ (5° by 5°, fig. S3) calculated from observations and $\Delta \ln A$ from AeroCom models (fig. S2), predictions for the geographic distributions of $\Delta \ln N_d$ and RF_{aci} using different aerosol quantities from various products are constructed in figs. S4 and S5, respectively. It is clear that substantial variations in $\beta_{A,PD}$, $\Delta \ln N_d$ and RF_{aci} exist not only between different proxies from the same product but also across different products for the same proxy. This suggests that both proxy selection and data biases [including measurement errors (*31*) and sampling biases (*24*)] play a role in determining RF_{aci}. Moreover, the limited accuracy of aerosol and cloud retrievals over land restricts the RF_{aci} estimates to oceanic regions (*22*, *31*, *34*). To extrapolate these estimates globally, a global-to-ocean RF_{aci} ratio from aerosol-climate models is commonly used (*22*), which, however, introduces yet another model-related uncertainty. These uncertainties, together with those associated with $\Delta \ln A$ and the methodologies used to determine $\beta_{A,PD}$ (Eq. 1), constitute the total observational RF_{aci} uncertainty. Note that the methodology-related uncertainty is not considered for here due to its complexity (*17*).

A wide range of different observational products and aerosol-climate models are used to decompose the RF_{aci} uncertainty into components (Fig. 4A and Materials and Methods). Here, the uncertainty is defined as the relative variation in RF_{aci} caused by corresponding uncertainty sources, quantified using the coefficient of variation (SD divided by mean) of a set of RF_{aci} estimates (Materials and Methods). Figure 4A shows that even without the methodology-related uncertainty, the combined uncertainty derived from the remaining four components is still estimated to be as high as 66%. The decomposition reveals that the proxy selection ("proxy_err") is a major source of uncertainty, resulting in 40% uncertainty on its own, while the observational biases in aerosol and N_d ("obs_err") only leads to 12% uncertainty, with the N_d component being minor (fig. S7), although our estimate in N_d uncertainty may be biased low because only MODerate-resolution Imaging Spectroradiometer (MODIS) N_d estimates are included in this study. Notably, model-driven uncertainties also make substantial contributions, with the uncertainty from $\Delta \ln A$ ("$\Delta \ln A$_err") being 36% and the uncertainty from the global-to-ocean RF_{aci} ratio ("land_ocean_err") being 20%. Note that the $\Delta \ln A$_err–related uncertainty also varies with the choice of proxy (fig. S7). A lower uncertainty is seen in sulfate-related proxies (~20%) owing to their relatively well-represented emissions and processes in climate models (*35*), while AI is more uncertain than the average (50%) because of the large diversity in modeled Ångström exponent (*27*).

The uncertainty caused by the proxy selection can be constrained by applying the observational scaling factors (δ_{obs}) presented in Fig. 3 (Fig. 4B). Applying this constraint yields a less negative RF_{aci} (−1.03 W m^{-2}) than the unconstrained case (−1.21 W m^{-2}). The 5 to 95% confidence range is substantially narrowed by ~40% from [−2.74 W m^{-2}, −0.33 W m^{-2}] to [−1.87 W m^{-2}, −0.48 W m^{-2}], thereby reducing the total uncertainty from 66 to 43%. The histogram of constrained RF_{aci} also exhibits less skewness, lowering the likelihood of a RF_{aci} more negative than −1.5 W m^{-2} (mainly contributed by SO4; fig. S5) and more positive than −0.5 W m^{-2} (primarily contributed by AOD; fig. S5). Applying the model-based scaling factor δ_{mod} similarly

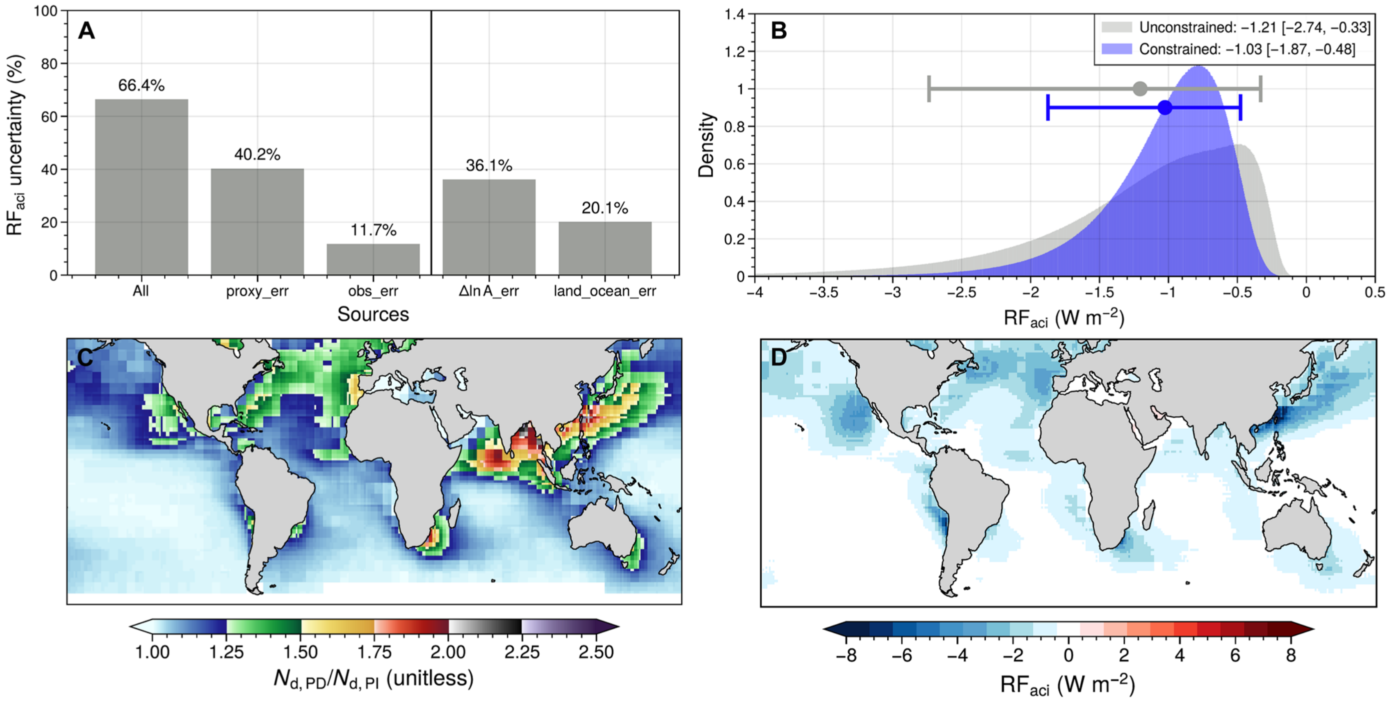

Fig. 4. Decomposing and constraining the uncertainty in Δln N_d and RF_{aci}. (**A**) The total uncertainty and the uncertainties from proxy selection (proxy_err), observational biases in both aerosol and N_d (obs_err), modeled Δln A (Δln A_err), and $RF_{aci}/RF_{aci,ocean}$ ratios (land_ocean_err). The two bars to the right of the vertical line correspond to model-related sources of uncertainty. (**B**) Histograms of global mean RF_{aci}: unconstrained (gray) and constrained by the optimal CCN choice based on δ_{obs} (blue). Mean values and 5th to 95th percentile uncertainty ranges are shown as error bars with dots. Spatial distributions of constrained (**C**) PD/PI N_d and (**D**) RF_{aci} over ocean. The ratio of PD to PI N_d is an exponential function of Δln N_d and is therefore directly linked to it.

reduces the uncertainty from 66 to 47%, yielding a best estimate of (−1.15 W m^{-2}; fig. S8). Table S1 summarizes RF_{aci} before and after the adjustment for each proxy, along with the values of δ_{obs} and δ_{mod} for use in future investigations.

Spatial distributions of constrained PD/PI N_d and RF_{aci} over ocean are shown in Fig. 4 (C and D). The most pronounced increase in N_d during the industrial era occurs over the northern Indian Ocean and the northern Pacific Ocean, with the PD/PI N_d ranging from 1.5 to 2.25, followed by the northern Atlantic Ocean, with the PD/PI N_d ranging from 1.25 to 1.5. In contrast, N_d remains largely unchanged throughout most of the pristine Southern Ocean, particularly the regions south of 30°S. This spatial pattern aligns with (*29*), justifying the use of the 30°S–60°S region as a proxy for the PI environment. The resulting RF_{aci} pattern generally mirrors the N_d change, with an exception over the northern Indian Ocean where liquid cloud fraction is very low (Fig. 4D).

These results demonstrate that, although some uncertainties remain difficult to constrain, applying the proxy constraint alone can efficiently reduce the uncertainty in global RF_{aci}, leading to a less negative RF_{aci} estimate. The remaining uncertainty is mainly from the model uncertainty in Δln A and the contribution over land, underscoring the crucial role of improving model representation for better observational estimates of RF_{aci}.

DISCUSSION

Building on a diverse suite of observational datasets and state-of-the-art aerosol–climate models, this work presented two approaches, hemispheric contrasts in N_d conditioned on aerosol and synthetic model experiments, to systematically evaluate the utility of various CCN proxies commonly used in recent research. The total uncertainty in RF_{aci} is quantified and subsequently decomposed into four key components, where the uncertainty due to the use of imperfect CCN proxies has been constrained by proposing a proxy-dependent correction factor.

Our results from hemispheric contrasts provide direct observational evidence that incorporating the information of aerosol size, hygroscopicity, and vertical profile into a proxy reduces the dependency of ln A–ln N_d relationships on the aerosol regime. We demonstrated that there does exist an aerosol quantity in current observational products that can evidently mitigate the aerosol-regime dependency issue, i.e., the reanalyzed CCN_b from CAMS (*33*). However, some residual dependency persists due to the limited accuracy of the CAMS CCN product tied to its host model, highlighting the need for further improvements in data quality.

The results from synthetic experiments offer a theoretical evaluation, not only determining the optimal proxy (i.e., CCN_s) in an error-free scenario but also quantifying the relative bias in RF_{aci} caused by inadequate proxies. This model-based bias (δ_{mod}) shows a good agreement with the observation-based bias (δ_{obs}), which justifies confidence in using δ_{obs} and/or δ_{mod} as emergent scaling factors, to adjust RF_{aci} obtained using any less-than-ideal proxies. This will be especially beneficial for proxies like AI and CCN_c, which, although lacking the cloud-base CCN information, can be retrieved with high accuracy from polarimetric measurements (*22*, *36*, *37*). Furthermore, the emergent scaling factors can also serve as a baseline for comparing and reconciling the diverse range of existing RF_{aci} estimates derived using different proxies, thereby facilitating a more consistent and robust understanding of RF_{aci}.

Our findings point to two practical pathways for further reducing the proxy-related uncertainty. The first is to refine the reanalysis CCN product, potentially by improving their underlying model representations or by assimilating aerosol size, hygroscopicity, and vertical profile information on top of AOD (*38*). The second is to apply the emergent scaling factors derived herein to the observations with higher accuracy.

The uncertainty decomposition identifies the proxy selection as the dominant source of uncertainty (40%), followed by $\Delta \ln A$ (36%), the global-to-ocean RF_{aci} ratio (20%), and observational biases in aerosol and N_d (12%). Applying the proxy constraint reduces the total uncertainty from 66 to 43%, and yields a less negative RFaci (-1.03 W m^{-2}) than the unconstrained case (-1.21 W m^{-2}), with a 5th to 95th percentile range of [-1.87 W m^{-2}, -0.48 W m^{-2}]. This result underscores the potential of proxy constraint to substantially reduce uncertainty in RF_{aci} estimates. As rapid adjustments approximately scale with RF_{aci}, our result is relevant for total ERF_{aci}, too.

A few potential caveats to decomposing and constraining should be noted. The total uncertainty in RF_{aci} presented here likely represents a lower bound of the actual uncertainty, as it does not include methodological uncertainties related to nonlinearity of the aerosol-N_d relation (*14*–*16*), cloud regime dependency (*31*, *39*), and aggregation scale (*40*). Notably, the nonlinear behavior alone was found to diminish the Twomey effect by 12 to 35% (*15*), which could be addressed in future work using nonlinear formulations, such as the sigmoid fit (*14*) or joint-histogram (*16*) approaches. In addition, the uncertainty related to observational biases may be a conservative lower bound, given that not all products are independent (e.g., MODIS is used as input for reanalysis data), and for N_d, we rely on only one product (MODIS), albeit using four of its variants derived from different sampling strategies (*19*).

The goal of future work should be to constrain the other identified uncertainty sources, in particular related to the PI-PD increase in CCN as well as the quantification of RF_{aci} over land. This challenge could be tackled by integrating new polarimetric and lidar satellite observations (*37*, *41*), data assimilation approaches (*38*), and model calibration techniques, such as perturbed parameter ensemble (PPE) (*42*). With new polarimetric measurements, we expect reduced measurement errors in both aerosol and N_d, particularly over land (*32*, *37*). This will not only directly reduce the uncertainty associated with observational errors but also eliminate the reliance on modeled ocean-to-global RF_{aci} ratios. In parallel, the data assimilation and PPE technique offer a powerful avenue for reducing model biases in aerosol emissions, properties, and processes. This, in turn, will help to reduce the uncertainty related to both ocean-to-global RF_{aci} ratios and $\Delta \ln A$.

MATERIALS AND METHODS

Observational data

The data of CCN proxies are taken from four different datasets with varying data uncertainties. Pure satellite products including the MODIS/Terra Collection 6.1 L3 data (*43*) and the POLarization and Directionality of Earth's Reflectance-3 (POLDER-3)/PARASOL L3 data, provide AOD and AI only. POLDER aerosol retrievals are from the SRON RemoTAP algorithm (*44*). Reanalysis products, the Modern-Era Retrospective analysis for Research and Applications version 2 (MERRA-2) (*45*) and CAMS ECMWF Atmospheric Composition Reanalysis 4 (*46*), offer not only AOD and AI but also continuous 3-D distributions of aerosol species. Sulfate column mass density ($SO4_c$) and surface mass concentrations ($SO4_s$) are directly from the reanalysis, while sulfate mass concentrations near the cloud base ($SO4_b$) are derived from sulfate vertical profiles from the reanalysis in combination with the cloud base height (CBH) retrievals from the Multi-angle Imaging SpectroRadiometer (MISR)/Terra L3 product (*47*). Note that AI is not directly provided in any dataset but is calculated as the product of AOD and the Ångström exponent (AI = AOD × Ångström exponent). Building on the CAMS reanalysis and a simplified kappa-Köhler framework (*33*) introduced a derived dataset providing 3-D CCN number concentrations at various supersaturations. Here, we use column-integrated (CCN_c), surface (CCN_s), and cloud-base CCN_b concentrations at 0.2% supersaturation, with CCN_b derived again from its vertical profile and CBH from MISR.

N_d retrievals come from a MODIS-based dataset (*48*) that provides N_d for single-layer liquid clouds with cloud top warmer than 268 K at a 1° by 1° resolution based on different sampling strategies. That is, N_d susceptibility is calculated from single-layer warm clouds, which account for 71% of all liquid-cloud scenes. The remaining multilayer and supercooled clouds, due to their larger retrieval uncertainties, are assumed to respond to aerosols similarly to the reliably retrieved single-layer warm clouds. To ensure a balance between accuracy and data coverage (*19*), we primarily use the N_d based on the strategy of (*32*) (referred to as G18), while also exploring the uncertainty caused by four different sampling strategies (*49*–*51*). The incoming solar radiation flux and the cloud albedo from the Clouds and the Earth's Radiant Energy System (CERES) and liquid cloud fraction (f_{liq}) from the MODIS/Terra L3 product are also used in the RF_{aci} calculation.

To cluster meteorological regimes (see below), the meteorological parameters closely linked to the liquid cloud formation including estimated inversion strength (EIS), vertical pressure velocity at 700 hPa (ω_{700}), relative humidity at 500 and 700 hPa (RH_{700} and RH_{500}), surface temperature and surface wind speed, from the European Centre for Medium-Range Weather Forecasts ERA5 reanalysis (*52*), are used as inputs of the clustering. EIS is not directly provided, instead is computed as

$$\mathrm{EIS} = \left(\theta_{700} - \theta_{1000}\right) - \Gamma_m^{850}\left(Z_{700} - Z_{\mathrm{LCL}}\right) \tag{2}$$

where are θ_{700} and θ_{1000} are the potential temperatures at 700 and 1000 hPa, Γ_m^{850} is the moist adiabatic lapse rate of potential temperature at 850 hPa, Z_{700} is the height at 700 hPa, and Z_{LCL} is the height of the lifting condensation level for an air parcel at the surface (*53*).

Different datasets vary in spatial and temporal resolution: MODIS, POLDER, CERES, and MISR L3 data are at a 1° by 1° resolution with daily frequency, while MERRA-2 is at a 0.5° by 0.625° resolution with 3-hourly frequency, CAMS data at a 0.75° by 0.75° resolution with 3-hourly frequency, and ERA5 at a 0.25° by 0.25° resolution with hourly frequency. Thus, all reanalysis data are regridded to 1° by 1° scale, and interpolated to 10:30 local solar time to approximate the overpass time of the Terra satellite. Four years (2006–2009) of the preprocessed data are then used for analysis. This study focuses on the global ocean between 60°S and 60°N due to the limited retrieval quality over land and polar regions.

Climate model data

Two major uses for model data in this study are deriving $\Delta \ln A$ for satellite-based RF_{aci} calculation and testing the consistency between β_{PD} and β_{PI-PD} in an idealized model world. Here, monthly mean aerosol and N_d fields in the PI and PD atmospheres are taken from global aerosol-climate simulations performed within the AeroCom model intercomparison projects (*25*–*27*), including AeroCom Phase II (AP2), Phase II IND3 (AP2_IND3), and Phase III (AP3) experiments. In these experiments, both PI (reference year 1850) and PD (reference year 2010) simulations are nudged to the PD horizontal winds and use the PD climatology for greenhouse gases, sea surface temperatures, and natural forcings, so that the PD-PI changes are solely attributed to the differing aerosol emissions. Unlike AP2 and AP3, which provide only aerosol outputs for the $\Delta \ln A$ estimation, AP2_IND3 also includes N_d fields, allowing us to diagnose and compare β_{PD} and β_{PI-PD}. Note that modeled CCN needs to be interpolated to supersaturation of 0.2% from 0.1% and 0.3%, to match CAMS CCN data. All model data are regridded to a same resolution of 1° by 1° for analysis. Table S2 summarizes the models used in this paper along with their available outputs. A total of 35 models provide a wide selection of model variants and microphysics schemes, allowing for an uncertainty assessment of RF_{aci} caused by the model uncertainty.

Clustering meteorological regime

To ensure the similar meteorological backgrounds between two hemispheres when contrasting N_d at a certain aerosol amount, we separate the meteorology into different regimes by applying the *k*-means clustering method (*54*) on the ERA5 meteorological parameters, including EIS, ω_{700}, RH_{700}, RH_{500}, surface temperature and surface wind speed. They are closely linked to the formation and development of warm clouds, known as cloud-controlling factors (*34*, *55*). A key parameter in the *k*-means clustering is the number of clusters (*k*). To find the optimal *k* the algorithm is run multiple times for $k = [2, 3, \ldots, 14]$, with 10,000 different random initializations for each *k*. For each run a set of metrics (inertia, Calinski-Harabasz index, silhouette score, Davies-Bouldin score, and SSE ratio) are calculated. Considering a balance of performance across all metrics, we end up with $k = 5$ as the optimal value. The geographic distributions of relative frequency of occurrence of the five clusters (fig. S1) show that C0 corresponds well to stratocumulus regions, C1 to trade wind cumulus regions, and C2 to convective cloud-dominated areas. Furthermore, C3 and C4 are associated with cold alto-class clouds and residual cloud types, which are therefore excluded from our analysis.

Quantifying hemispheric contrasts in N_d

In the analysis of hemispheric contrast, the NH and SH are defined as the oceans between 30°N–60°N and 30°S–60°S, respectively, to ensure a sufficient hemispheric difference in aerosol background (*29*, *30*). The data of N_d and CCN proxies (*A*) are first grouped into 40 bins with fixed intervals of $\ln A$. To facilitate the comparison across all proxies, we define a metric $\Delta N_{d|SH-NH|}$ to quantify the hemispheric contrast

$$\Delta N_{d|SH-NH|} = \sum_{i=1}^{40} \omega_i \left| \frac{N_{d(SH),i} - N_{d(NH),i}}{N_{d(Glob),i}} \right| \times 100\% \tag{3}$$

where $N_{d(SH),i}$ and $N_{d(NH),i}$ are the median N_d values in the *i*th aerosol bin over the SH and NH, respectively, while $N_{d(Glob),i}$ is the median N_d in the *i*th bin over entire selected ocean. The absolute value of the difference is taken to avoid cancellation of positive and negative differences. In addition, the relative difference in each bin is weighted by the sample size of the hemisphere with fewer data in that bin (ω_i), to account for the comparability between two hemispheres.

Diagnosing N_d susceptibility

The N_d susceptibility to aerosols is diagnosed separately for (i) calculating observation-based RF_{aci} and (ii) comparing $\beta_{A,PD}$ and $\beta_{A,PI-PD}$ in an idealized model world.

For the first purpose, $\beta_{A,PD}$ is calculated at each 5° by 5° grid using daily MODIS G18 N_d and 14 CCN proxies (denoted as *A*) from different products (fig. S3)

$$\beta_{A,PD} = \frac{d\ln N_d}{d\ln A} \tag{4}$$

It is known that a weak aerosol optical signal under clean conditions artificially produces a shallow $\ln A$–$\ln N_d$ zone (*22*) in the satellite-derived relationship, biasing $\beta_{A,PD}$ toward a lower value. A similar issue should also appear in reanalysis products as they assimilate satellite retrievals. Thus, data within this shallow zone are excluded to minimize this bias. To determine the cutoff value, we first fit a sigmoidal curve to each $\ln A$–$\ln N_d$ following (*14*), and define the cutoff value as the value of *A* where the derivative of curve starts reaching 0.05.

For the second purpose, the $\beta_{A,PD}$ is calculated from monthly gridded model outputs according to Eq. 4. The $\beta_{A,PI-PD}$ is diagnosed using global mean $\ln N_d$ and $\ln A$ in the PI and PD atmospheres

$$\beta_{A,PI-PD} = \frac{\overline{\ln N_{d,PD}} - \overline{\ln N_{d,PI}}}{\overline{\ln A_{PD}} - \overline{\ln A_{PI}}} \tag{5}$$

where the overbar denotes a global average. The calculation here is based on multimodel mean from six AeroCom AP2_IND3 models (table S2). As the AP2_IND3 does not provide SO4-related outputs, the corresponding $\beta_{A,PD}$ and $\beta_{A,PI-PD}$ are inferred by combining multimodel mean $SO4_c$ and $SO4_s$ from AP2 and AP3 with multimodel mean N_d from the AP2_IND3 experiments. To ensure consistency with satellite-based estimates, the model data are also restricted to the global ocean between 60°S and 60°N.

Estimating RF_{aci} and its bias

The estimation of RF_{aci} (the Twomey effect) follows a chain of physical processes from anthropogenic perturbation to N_d caused by PI-PD aerosol change, via cloud albedo response to $\Delta \ln N_d$ (*56*), to radiation change over liquid clouds (*57*)

$$RF_{aci} = -F^{\downarrow} f_{liq} \frac{\alpha_{cld}\left(1-\alpha_{cld}\right)}{3} \Delta \ln N_d \tag{6}$$

where $F^{\downarrow}$ is the incoming solar radiation flux, α_{cld} is the cloud albedo (both from CERES), and f_{liq} is the liquid cloud fraction from MODIS. $\Delta \ln N_d$ is determined from the observation-derived $\beta_{A,PD}$ and modeled $\Delta \ln A$ according to Eq. 1, where the reference years for PI and PD are 1850 and 2010, respectively. Because of the large retrieval uncertainty over land, RF_{aci} is only calculated over ocean ($RF_{aci,ocean}$). To extend the estimation to the entire globe, we use the ratios $RF_{aci}/RF_{aci,ocean}$ from 13 different aerosol–climate models in (*5*), ranging from 1.12 to 2.24 with a mean of 1.5 (*22*).

The relative bias in RF_{aci} diagnosed from observations is calculated assuming CCN_s to be the baseline of true RF_{aci}

$$\delta_{obs} = \frac{RF_{aci,A} - RF_{aci,CCNs}}{RF_{aci,CCNs}} \times 100\% \quad (7)$$

where $RF_{aci,A}$ and $RF_{aci,CCNs}$ are the RF_{aci} derived using proxy A and CCN_s. Here, $RF_{aci,A}$ is calculated as the average across different products (fig. S5). To isolate the effect of proxy selection from differing $\Delta \ln A$ across various models, only two AeroCom models, ECHAM-HAM and HadGEM3-A-GLOMAP, are used, as they provide outputs for all considered proxies.

In the synthetic experiments, the relative bias in RF_{aci} can be approximated to be the relative deviation of $\beta_{A,PD}$ from $\beta_{A,PI-PD}$ as β is linearly related to RF_{aci} (Eq. 1)

$$\delta_{mod} = \frac{\beta_{A,PD} - \beta_{A,PI-PD}}{\beta_{A,PI-PD}} \times 100\% \quad (8)$$

Decomposing RF_{aci} uncertainty

The uncertainty in RF_{aci} originates from (1) the choice of CCN proxies, (2) observational biases across various datasets, (3) RF_{aci}/$RF_{aci,ocean}$ ratios, (4) uncertainties in modeled $\Delta \ln A$, and (5) the methodology used to determine β (*17*, *57*). This study focuses only on (1) to (4), since the last source involves multiple aspects beyond the scope of this work. The relative uncertainty (diversity) is quantified as the coefficient of variation (CV × 100%, SD divided by mean) of a set of RF_{aci} estimates, following established practice in AeroCom model evaluation studies (*27*).

The combined effects of proxy selection and observational biases (sources 1 and 2) are reflected in the variability of 56 $RF_{aci,ocean}$ values derived from the combination of 14 aerosol quantities (from different products) × 4 N_d quantities (from different sampling strategies) with varying degrees of bias. The uncertainty due to proxy choice alone is represented by the variability of six $RF_{aci,ocean}$ values derived from different proxies (AOD, AI, $SO4_c$, $SO4_s$, CCN_c, and CCN_s) averaged over products. The uncertainty due to observational biases alone is the same as the combined variability from sources (1) and (2) but adjusted to the CCN_s level using scaling factors (δ_{obs}) given in Fig. 3. The uncertainty in RF_{aci}/$RF_{aci,ocean}$ ratios (source 3), is captured by 13 RF_{aci}/$RF_{aci,ocean}$ ratios from different models (*22*). For source (4), we simulate the uncertainty in $\Delta \ln A$ with a log-normal distribution of RF_{aci} scaling factors with a mean of 1, a SD (σ) of 0.36, and a sample size of 100,000, where σ is based on the averaged uncertainty caused solely by model uncertainty (cyan dashed line in fig. S7). Combining this simulated distribution with the 56 $RF_{aci,ocean}$ values without adjusting and the 13 RF_{aci}/$RF_{aci,ocean}$ ratios, we generate a histogram of possible global mean RF_{aci} values (Fig. 4B), representing total uncertainty caused by sources (1) to (4). To isolate the uncertainty contributed by each individual source, we use a controlled variation method, holding all other sources constant at their mean values while allowing only the source of interest to vary. The resulting histograms are then used to quantify the corresponding uncertainty (Fig. 4A).

Supplementary Materials

This PDF file includes:
Figs. S1 to S8
Tables S1 and S2

REFERENCES

1. P. Forster, T. Storelvmo, K. Armour, W. Collins, J.-L. Dufresne, D. Frame, D.J. Lunt, T. Mauritsen, M.D. Palmer, M. Watanabe, M. Wild, H. Zhang, The Earth's Energy Budget, Climate Feedbacks, and Climate Sensitivity, in *Climate Change 2021: The Physical Science Basis. Contribution of Working Group I to the Sixth Assessment Report of the Intergovernmental Panel on Climate Change*, V. Masson-Delmotte, et al., Eds. (Cambridge Univ. Press, Cambridge, United Kingdom and New York, NY, USA, 2021), chap. 7, pp. 923–1054; 10.1017/9781009157896.009.
2. S. Twomey, Pollution and the planetary albedo. *Atmos. Environ.* **8**, 1251–1256 (1974).
3. A. S. Ackerman, M. P. Kirkpatrick, D. E. Stevens, O. B. Toon, The impact of humidity above stratiform clouds on indirect aerosol climate forcing. *Nature* **432**, 1014–1017 (2004).
4. B. A. Albrecht, Aerosols, cloud microphysics, and fractional cloudiness. *Science* **245**, 1227–1230 (1989).
5. E. Gryspeerdt, T. Goren, O. Sourdeval, J. Quaas, J. Mülmenstädt, S. Dipu, C. Unglaub, A. Gettelman, M. Christensen, Constraining the aerosol influence on cloud liquid water path. *Atmos. Chem. Phys.* **19**, 5331–5347 (2019).
6. Y. Chen, J. Haywood, Y. Wang, F. Malavelle, G. Jordan, D. Partridge, J. Fieldsend, J. De Leeuw, A. Schmidt, N. Cho, L. Oreopoulos, S. Platnick, D. Grosvenor, P. Field, U. Lohmann, Machine learning reveals climate forcing from aerosols is dominated by increased cloud cover. *Nat. Geosci.* **15**, 609–614 (2022).
7. T. Yuan, H. Song, R. Wood, L. Oreopoulos, S. Platnick, C. Wang, H. Yu, K. Meyer, E. Wilcox, Observational evidence of strong forcing from aerosol effect on low cloud coverage. *Sci. Adv.* **9**, eadh7716 (2023).
8. A. Tippett, E. Gryspeerdt, P. Manshausen, P. Stier, T. W. P. Smith, Weak liquid water path response in ship tracks. *Atmos. Chem. Phys.* **24**, 13269–13283 (2024).
9. N. Bellouin, J. Quaas, E. Gryspeerdt, S. Kinne, P. Stier, D. Watson-Parris, O. Boucher, K. S. Carslaw, M. Christensen, A.-L. Daniau, J.-L. Dufresne, G. Feingold, S. Fiedler, P. Forster, A. Gettelman, J. M. Haywood, U. Lohmann, F. Malavelle, T. Mauritsen, D. T. McCoy, G. Myhre, J. Mülmenstädt, D. Neubauer, A. Possner, M. Rugenstein, Y. Sato, M. Schulz, S. E. Schwartz, O. Sourdeval, T. Storelvmo, V. Toll, D. Winker, B. Stevens, Bounding global aerosol radiative forcing of climate change. *Rev. Geophys.* **58**, e2019RG000660 (2020).
10. E. Gryspeerdt, J. Mülmenstädt, A. Gettelman, F. F. Malavelle, H. Morrison, D. Neubauer, D. G. Partridge, P. Stier, T. Takemura, H. Wang, M. Wang, K. Zhang, Surprising similarities in model and observational aerosol radiative forcing estimates. *Atmos. Chem. Phys.* **20**, 613–623 (2020).
11. T. Nakajima, A. Higurashi, K. Kawamoto, J. E. Penner, A possible correlation between satellite-derived cloud and aerosol microphysical parameters. *Geophys. Res. Lett.* **28**, 1171–1174 (2001).
12. M. Sekiguchi, T. Nakajima, K. Suzuki, K. Kawamoto, A. Higurashi, D. Rosenfeld, I. Sano, S. Mukai, A study of the direct and indirect effects of aerosols using global satellite data sets of aerosol and cloud parameters. *J. Geophys. Res. Atmos.* **108**, 4699 (2003).
13. J. Quaas, O. Boucher, N. Bellouin, S. Kinne, Satellite-based estimate of the direct and indirect aerosol climate forcing. *J. Geophys. Res. Atmos.* **113**, D05204 (2008).
14. H. Jia, J. Quaas, Nonlinearity of the cloud response postpones climate penalty of mitigating air pollution in polluted regions. *Nat. Clim. Change* **13**, 943–950 (2023).
15. J. L. Dedrick, C. N. Pelayo, L. M. Russell, D. Lubin, J. Mülmenstädt, M. Miller, Competition response of cloud supersaturation explains diminished Twomey effect for smoky aerosol in the tropical Atlantic. *Proc. Natl. Acad. Sci. U.S.A.* **122**, e2412247122 (2025).
16. E. Gryspeerdt, J. Quaas, S. Ferrachat, A. Gettelman, S. Ghan, U. Lohmann, H. Morrison, D. Neubauer, D. G. Partridge, P. Stier, T. Takemura, H. Wang, M. Wang, K. Zhang, Constraining the instantaneous aerosol influence on cloud albedo. *Proc. Natl. Acad. Sci. U.S.A.* **114**, 4899–4904 (2017).
17. D. Rosenfeld, A. Kokhanovsky, T. Goren, E. Gryspeerdt, O. Hasekamp, H. Jia, A. Lopatin, J. Quaas, Z. Pan, O. Sourdeval, Frontiers in satellite-based estimates of cloud-mediated aerosol forcing. *Rev. Geophys.* **61**, e2022RG000799 (2023).
18. A. Virtanen, J. Joutsensaari, H. Kokkola, D. G. Partridge, S. Blichner, Ø. Seland, E. Holopainen, E. Tovazzi, A. Lipponen, S. Mikkonen, A. Leskinen, A. P. Hyvärinen, P. Zieger, R. Krejci, A. M. L. Ekman, I. Riipinen, J. Quaas, S. Romakkaniemi, High sensitivity of cloud formation to aerosol changes. *Nat. Geosci.* **18**, 289–295 (2025).
19. E. Gryspeerdt, D. T. McCoy, E. Crosbie, R. H. Moore, G. J. Nott, D. Painemal, J. Small-Griswold, A. Sorooshian, L. Ziemba, The impact of sampling strategy on the cloud droplet number concentration estimated from satellite data. *Atmos. Meas. Tech.* **15**, 3875–3892 (2022).
20. B. Zhao, Y. Gu, K. N. Liou, Y. Wang, X. Liu, L. Huang, J. H. Jiang, H. Su, Type-dependent responses of ice cloud properties to aerosols from satellite retrievals. *Geophys. Res. Lett.* **45**, 3297–3306 (2018).
21. J. H. Seinfeld, C. Bretherton, K. S. Carslaw, H. Coe, P. J. De Mott, E. J. Dunlea, G. Feingold, S. Ghan, A. B. Guenther, R. Kahn, I. Kraucunas, S. M. Kreidenweis, M. J. Molina, A. Nenes, J. E. Penner, K. A. Prather, V. Ramanathan, V. Ramaswamy, P. J. Rasch, A. R. Ravishankara, D. Rosenfeld, G. Stephens, R. Wood, Improving our fundamental understanding of the role of aerosol–cloud interactions in the climate system. *Proc. Natl. Acad. Sci. U.S.A.* **113**, 5781–5790 (2016).

22. O. P. Hasekamp, E. Gryspeerdt, J. Quaas, Analysis of polarimetric satellite measurements suggests stronger cooling due to aerosol-cloud interactions. *Nat. Commun.* **10**, 5405 (2019).
23. P. Stier, Limitations of passive remote sensing to constrain global cloud condensation nuclei. *Atmos. Chem. Phys.* **16**, 6595–6607 (2016).
24. H. Jia, X. Ma, F. Yu, J. Quaas, Significant underestimation of radiative forcing by aerosol–cloud interactions derived from satellite-based methods. *Nat. Commun.* **12**, 3649 (2021).
25. G. Myhre, B. H. Samset, M. Schulz, Y. Balkanski, S. Bauer, T. K. Berntsen, H. Bian, N. Bellouin, M. Chin, T. Diehl, R. C. Easter, J. Feichter, S. J. Ghan, D. Hauglustaine, T. Iversen, S. Kinne, A. Kirkevåg, J.-F. Lamarque, G. Lin, X. Liu, M. T. Lund, G. Luo, X. Ma, T. van Noije, J. E. Penner, P. J. Rasch, A. Ruiz, Ø. Seland, R. B. Skeie, P. Stier, T. Takemura, K. Tsigaridis, P. Wang, Z. Wang, L. Xu, H. Yu, F. Yu, J.-H. Yoon, K. Zhang, H. Zhang, C. Zhou, Radiative forcing of the direct aerosol effect from AeroCom Phase II simulations. *Atmos. Chem. Phys.* **13**, 1853–1877 (2013).
26. S. Ghan, M. Wang, S. Zhang, S. Ferrachat, A. Gettelman, J. Griesfeller, Z. Kipling, U. Lohmann, H. Morrison, D. Neubauer, D. G. Partridge, P. Stier, T. Takemura, H. Wang, K. Zhang, Challenges in constraining anthropogenic aerosol effects on cloud radiative forcing using present-day spatiotemporal variability. *Proc. Natl. Acad. Sci. U.S.A.* **113**, 5804–5811 (2016).
27. J. Gliß, A. Mortier, M. Schulz, E. Andrews, Y. Balkanski, S. E. Bauer, A. M. K. Benedictow, H. Bian, R. Checa-Garcia, M. Chin, P. Ginoux, J. J. Griesfeller, A. Heckel, Z. Kipling, A. Kirkevåg, H. Kokkola, P. Laj, P. L. Sager, M. T. Lund, C. L. Myhre, H. Matsui, G. Myhre, D. Neubauer, T. van Noije, P. North, D. J. L. Olivié, S. Rémy, L. Sogacheva, T. Takemura, K. Tsigaridis, S. G. Tsyro, AeroCom phase III multi-model evaluation of the aerosol life cycle and optical properties using ground- and space-based remote sensing as well as surface in situ observations. *Atmos. Chem. Phys.* **21**, 87–128 (2021).
28. J. E. Penner, L. Xu, M. Wang, Satellite methods underestimate indirect climate forcing by aerosols. *Proc. Natl. Acad. Sci. U.S.A.* **108**, 13404–13408 (2011).
29. D. S. Hamilton, L. A. Lee, K. J. Pringle, C. L. Reddington, D. V. Spracklen, K. S. Carslaw, Occurrence of pristine aerosol environments on a polluted planet. *Proc. Natl. Acad. Sci. U.S.A.* **111**, 18466–18471 (2014).
30. I. L. McCoy, D. T. Mccoy, R. Wood, L. Regayre, D. Watson-Parris, D. P. Grosvenor, J. Mulcahy, Y. Hu, F. Bender, P. R. Field, K. S. Carslaw, H. Gordon, The hemispheric contrast in cloud microphysical properties constrains aerosol forcing. *Proc. Natl. Acad. Sci. U.S.A.* **117**, 18998–19006 (2020).
31. H. Jia, J. Quaas, E. Gryspeerdt, C. Böhm, O. Sourdeval, Addressing the difficulties in quantifying droplet number response to aerosol from satellite observations. *Atmos. Chem. Phys.* **22**, 7353–7372 (2022).
32. D. P. Grosvenor, O. Sourdeval, P. Zuidema, A. Ackerman, M. D. Alexandrov, R. Bennartz, R. Boers, B. Cairns, J. C. Chiu, M. Christensen, H. Deneke, M. Diamond, G. Feingold, A. Fridlind, A. Hünerbein, C. Knist, P. Kollias, A. Marshak, D. McCoy, D. Merk, D. Painemal, J. Rausch, D. Rosenfeld, H. Russchenberg, P. Seifert, K. Sinclair, P. Stier, B. van Diedenhoven, M. Wendisch, F. Werner, R. Wood, Z. Zhang, J. Quaas, Remote sensing of droplet number concentration in warm clouds: A review of the current state of knowledge and perspectives. *Rev. Geophys.* **56**, 409–453 (2018).
33. K. Block, M. Haghighatnasab, D. G. Partridge, P. Stier, J. Quaas, Cloud condensation nuclei concentrations derived from the CAMS reanalysis. *Earth Syst. Sci. Data* **16**, 443–470 (2024).
34. C. J. Wall, J. R. Norris, A. Possner, D. T. McCoy, I. L. McCoy, N. J. Lutsko, Assessing effective radiative forcing from aerosol–cloud interactions over the global ocean. *Proc. Natl. Acad. Sci. U.S.A.* **119**, e2210481119 (2022).
35. C. Textor, M. Schulz, S. Guibert, S. Kinne, Y. Balkanski, S. Bauer, T. Berntsen, T. Berglen, O. Boucher, M. Chin, F. Dentener, T. Diehl, R. Easter, H. Feichter, D. Fillmore, S. Ghan, P. Ginoux, S. Gong, A. Grini, J. Hendricks, L. Horowitz, P. Huang, I. Isaksen, I. Iversen, S. Kloster, D. Koch, A. Kirkevåg, J. E. Kristjansson, M. Krol, A. Lauer, J. F. Lamarque, X. Liu, V. Montanaro, G. Myhre, J. Penner, G. Pitari, S. Reddy, Ø. Seland, P. Stier, T. Takemura, X. Tie, Analysis and quantification of the diversities of aerosol life cycles within AeroCom. *Atmos. Chem. Phys.* **6**, 1777–1813 (2006).
36. O. P. Hasekamp, G. Fu, S. P. Rusli, L. Wu, A. D. Noia, J. aan de Brugh, J. Landgraf, J. M. Smit, J. Rietjens, A. van Amerongen, Aerosol measurements by SPEXone on the NASA PACE mission: Expected retrieval capabilities. *J. Quant. Spectrosc. Radiat. Transfer* **227**, 170–184 (2019).
37. G. Fu, J. Rietjens, R. Laasner, L. van der Schaaf, R. van Hees, Z. Yuan, B. van Diedenhoven, N. Hannadige, J. Landgraf, M. Smit, K. Knobelspiesse, B. Cairns, M. Gao, B. Franz, J. Werdell, O. Hasekamp, Aerosol retrievals from SPEXone on the NASA PACE mission: First results and validation. *Geophys. Res. Lett.* **52**, e2024GL113525 (2025).
38. A. Tsikerdekis, O. P. Hasekamp, N. A. J. Schutgens, Q. Zhong, Assimilation of POLDER observations to estimate aerosol emissions. *Atmos. Chem. Phys.* **23**, 9495–9524 (2023).
39. Y.-C. Chen, M. W. Christensen, G. L. Stephens, J. H. Seinfeld, Satellite-based estimate of global aerosol–cloud radiative forcing by marine warm clouds. *Nat. Geosci.* **7**, 643–646 (2014).
40. B. S. Grandey, P. Stier, A critical look at spatial scale choices in satellite-based aerosol indirect effect studies. *Atmos. Chem. Phys.* **10**, 11459–11470 (2010).
41. T. Wehr, T. Kubota, G. Tzeremes, K. Wallace, H. Nakatsuka, Y. Ohno, R. Koopman, S. Rusli, M. Kikuchi, M. Eisinger, T. Tanaka, M. Taga, P. Deghaye, E. Tomita, D. Bernaerts, The EarthCARE mission–Science and system overview. *Atmos. Meas. Tech.* **16**, 3581–3608 (2023).
42. L. A. Regayre, L. Deaconu, D. P. Grosvenor, D. M. H. Sexton, C. Symonds, T. Langton, D. Watson-Paris, J. P. Mulcahy, K. J. Pringle, M. Richardson, J. S. Johnson, J. W. Rostron, H. Gordon, G. Lister, P. Stier, K. S. Carslaw, Identifying climate model structural inconsistencies allows for tight constraint of aerosol radiative forcing. *Atmos. Chem. Phys.* **23**, 8749–8768 (2023).
43. R. C. Levy, S. Mattoo, L. A. Munchak, L. A. Remer, A. M. Sayer, F. Patadia, N. C. Hsu, The Collection 6 MODIS aerosol products over land and ocean. *Atmos. Meas. Tech.* **6**, 2989–3034 (2013).
44. O. Hasekamp, P. Litvinov, G. Fu, C. Chen, O. Dubovik, Algorithm evaluation for polarimetric remote sensing of atmospheric aerosols. *Atmos. Meas. Tech.* **17**, 1497–1525 (2024).
45. C. A. Randles, A. M. Da Silva, V. Buchard, P. R. Colarco, A. Darmenov, R. Govindaraju, A. Smirnov, B. Holben, R. Ferrare, J. Hair, Y. Shinozuka, C. J. Flynn, The MERRA-2 aerosol reanalysis, 1980 onward. Part I: System description and data assimilation evaluation. *J. Climate* **30**, 6823–6850 (2017).
46. A. Inness, M. Ades, A. Agustí-Panareda, J. Barré, A. Benedictow, A.-M. Blechschmidt, J. J. Dominguez, R. Engelen, H. Eskes, J. Flemming, V. Huijnen, L. Jones, Z. Kipling, S. Massart, M. Parrington, V.-H. Peuch, M. Razinger, S. Remy, M. Schulz, M. Suttie, The CAMS reanalysis of atmospheric composition. *Atmos. Chem. Phys.* **19**, 3515–3556 (2019).
47. C. Böhm, O. Sourdeval, J. Mülmenstädt, J. Quaas, S. Crewell, Cloud base height retrieval from multi-angle satellite data. *Atmos. Meas. Tech.* **12**, 1841–1860 (2019).
48. E. Gryspeerdt, D. M. Coy, E. Crosbie, R. H. Moore, G. J. Nott, D. Painemal, J. Small-Griswold, A. Sorooshian, L. Ziemba, Cloud droplet number concentration, calculated from the MODIS (Moderate resolution imaging spectroradiometer) cloud optical properties retrieval and gridded using different sampling strategies (2022); https://doi.org/10.5285/864a46cc65054008857ee5bb772a2a2b.
49. R. Bennartz, J. Rausch, Global and regional estimates of warm cloud droplet number concentration based on 13 years of AQUA-MODIS observations. *Atmos. Chem. Phys.* **17**, 9815–9836 (2017).
50. J. Quaas, O. Boucher, U. Lohmann, Constraining the total aerosol indirect effect in the LMDZ and ECHAM4 GCMs using MODIS satellite data. *Atmos. Chem. Phys.* **6**, 947–955 (2006).
51. Y. Zhu, D. Rosenfeld, Z. Li, Under what conditions can we trust retrieved cloud drop concentrations in broken marine stratocumulus? *J. Geophys. Res. Atmos.* **123**, 8754–8767 (2018).
52. H. Hersbach, B. Bell, P. Berrisford, S. Hirahara, A. Horányi, J. Muñoz-Sabater, J. Nicolas, C. Peubey, R. Radu, D. Schepers, A. Simmons, C. Soci, S. Abdalla, X. Abellan, G. Balsamo, P. Bechtold, G. Biavati, J. Bidlot, M. Bonavita, G. De Chiara, P. Dahlgren, D. Dee, M. Diamantakis, R. Dragani, J. Flemming, R. Forbes, M. Fuentes, A. Geer, L. Haimberger, S. Healy, R. J. Hogan, E. Hólm, M. Janisková, S. Keeley, P. Laloyaux, P. Lopez, C. Lupu, G. Radnoti, P. de Rosnay, I. Rozum, F. Vamborg, S. Villaume, J.-N. Thépaut, The ERA5 global reanalysis. *Q. J. Roy. Meteorol. Soc.* **146**, 1999–2049 (2020).
53. R. Wood, C. S. Bretherton, On the relationship between stratiform low cloud cover and lower-tropospheric stability. *J. Climate* **19**, 6425–6432 (2006).
54. M. R. Anderberg, Cluster analysis for applications, in *Cluster Analysis for Application* (Academic Press, New York, 1973), p. 359.
55. S. A. Klein, A. Hall, J. R. Norris, R. Pincus, Low-cloud feedbacks from cloud-controlling factors: A review. *Surv. Geophys.* **38**, 1307–1329 (2017).
56. S. Twomey, Aerosols, clouds and radiation. *Atmos. Environ.* **25**, 2435–2442 (1991).
57. J. Quaas, A. Arola, B. Cairns, M. Christensen, H. Deneke, A. M. L. Ekman, G. Feingold, A. Fridlind, E. Gryspeerdt, O. Hasekamp, Z. Li, A. Lipponen, P.-L. Ma, J. Mülmenstädt, A. Nenes, J. E. Penner, D. Rosenfeld, R. Schrödner, K. Sinclair, O. Sourdeval, P. Stier, M. Tesche, B. van Diedenhoven, M. Wendisch, Constraining the Twomey effect from satellite observations: Issues and perspectives. *Atmos. Chem. Phys.* **20**, 15079–15099 (2020).

Acknowledgments: We thank all data producers for making the datasets available, and AeroCom modelers for preparing and submitting model outputs. We also thank M. Schulz and A. Benedictow at the Norwegian Meteorological Institute for the assistance in accessing the AeroCom server. **Funding:** This research was funded by the Horizon Europe program through the projects CleanCloud (GA 101137639 to H.J., J.Q., B.v.D., and O.H.) and CERTAINTY (GA 101137680 to E.G.), and by the Dutch Research Council (NWO) through the project ACIaction (file no. OCENW.M.24.024 to H.J.; https://doi.org/10.61686/OZRJI30024). This work was also supported by the Dutch national e-infrastructure with computing resources provided by the SURF Cooperative (grant no. EINF8447 to H.J.). E.G. was supported by an Imperial College Junior Research Fellowship and a Royal Society University Research Fellowship (URF/R1/191602).

C.B. was support by the Deutsche Forschungsgemeinschaft (DFG, German Research Foundation), project number 268236062, SFB 1211. **Author contributions:** Writing–original draft: H.J. Conceptualization: H.J., J.Q., O.H., and B.v.D. Investigation: H.J., O.H., and J.Q. Writing–review and editing: H.J., O.H., J.Q., E.G., B.v.D., K.B., and C.B. Methodology: H.J., W.K., and O.H. Resources: H.J., O.H., and B.v.D. Funding acquisition: H.J. and O.H. Data curation: H.J. and C.B. Validation: H.J. Formal analysis: H.J. and W.K. Software: H.J., W.K., and C.B. Project administration: H.J. Visualization: H.J. and W.K. **Competing interests:** The authors declare that they have no competing interests. **Data, code, and materials availability:** The MODIS Level 3 products are available from the Atmosphere Archive and Distribution System (LAADS) Distributed Active Archive Center (DAAC): https://ladsweb.modaps.eosdis.nasa.gov/archive/allData/61/MOD08_D3/. The POLDER-3/PARASOL polarimetric retrievals by the SRON RemoTAP algorithm are available from SRON at www.sron.nl/harpol. The MODIS-based N_d dataset with different sampling strategies are available from the Centre for Environmental Data Analysis at https://doi.org/10.5285/864a46cc65054008857ee5bb772a2a2b. The CERES SSF Level 3 products are obtained from the NASA Langley Research Center CERES ordering tool at https://ceres.larc.nasa.gov/data/. The MISR Cloud Product are from https://doi.org/10.5880/CRC1211DB.19. The MERRA-2 and ERA5 reanalysis products are collected from https://goldsmr4.gesdisc.eosdis.nasa.gov/data/MERRA2/ and https://www.ecmwf.int/en/forecasts/dataset/ecmwf-reanalysis-v5. The CAMS aerosol concentrations are available from the CAMS Atmosphere Data Store (ADS) (https://ads.atmosphere.copernicus.eu/datasets/cams-global-reanalysis-eac4?tab=download), and the CAMS-derived CCN data can be downloaded from https://doi.org/10.26050/WDCC/QUAERERE_CCNCAMS_v1. This study did not generate new materials. All data and code needed to evaluate and reproduce the results in the paper are present in the paper and/or the Supplementary Materials.

Submitted 11 July 2025
Accepted 14 January 2026
Published 18 February 2026
10.1126/sciadv.aea4828

Science Advances

Optimal choice of proxy for cloud condensation nuclei reduces uncertainty in aerosol-cloud-climate forcing

Hailing Jia, Johannes Quaas, Willem Kroese, Bastiaan van Diedenhoven, Edward Gryspeerdt, Christoph Böhm, Karoline Block, and Otto Hasekamp

Sci. Adv. **12** (8), eaea4828. DOI: 10.1126/sciadv.aea4828

Science Advances (ISSN 2375-2548) is published by the American Association for the Advancement of Science. 1200 New York Avenue NW, Washington, DC 20005. The title *Science Advances* is a registered trademark of AAAS.